Comptes Rendus
Géoscience — Sciences de la Planète
Supplementary material to the article available at:
https://doi.org/10.5802/crgeos.78

Seismicity in France / *Sismicité en France*

Supplementary material: Constraining the point source parameters of the 11 November 2019 Mw 4.9 Le Teil earthquake using multiple relocation approaches, first motion and full waveform inversions

Bertrand Delouis*, [a], Elif Oral [a], Marine Menager [a, b], Jean-Paul Ampuero [a], Aurélie Guilhem Trilla [b], Marc Régnier [a] and Anne Deschamps [a]

[a] Université Côte d'Azur, IRD, CNRS, Observatoire de la Côte d'Azur, Géoazur, 250 rue Albert Einstein, 06560 Valbonne, France

[b] CEA, DAM, DIF, F-91297 Arpajon, France

Current address: CNRS-GEOAZUR, Campus Azur, 250 rue Albert Einstein, CS 10269, 06905 Sophia Antipolis Cedex, France (B. Delouis)

E-mails: delouis@geoazur.unice.fr (B. Delouis), oral.elif@yahoo.com (E. Oral), Marine.MENAGER@cea.fr (M. Menager), ampuero@geoazur.unice.fr (J.-P. Ampuero), Aurelie.TRILLA@cea.fr (A. Guilhem Trilla), Marc.REGNIER@geoazur.unice.fr (M. Régnier), deschamps@geoazur.unice.fr (A. Deschamps)

* Corresponding author.

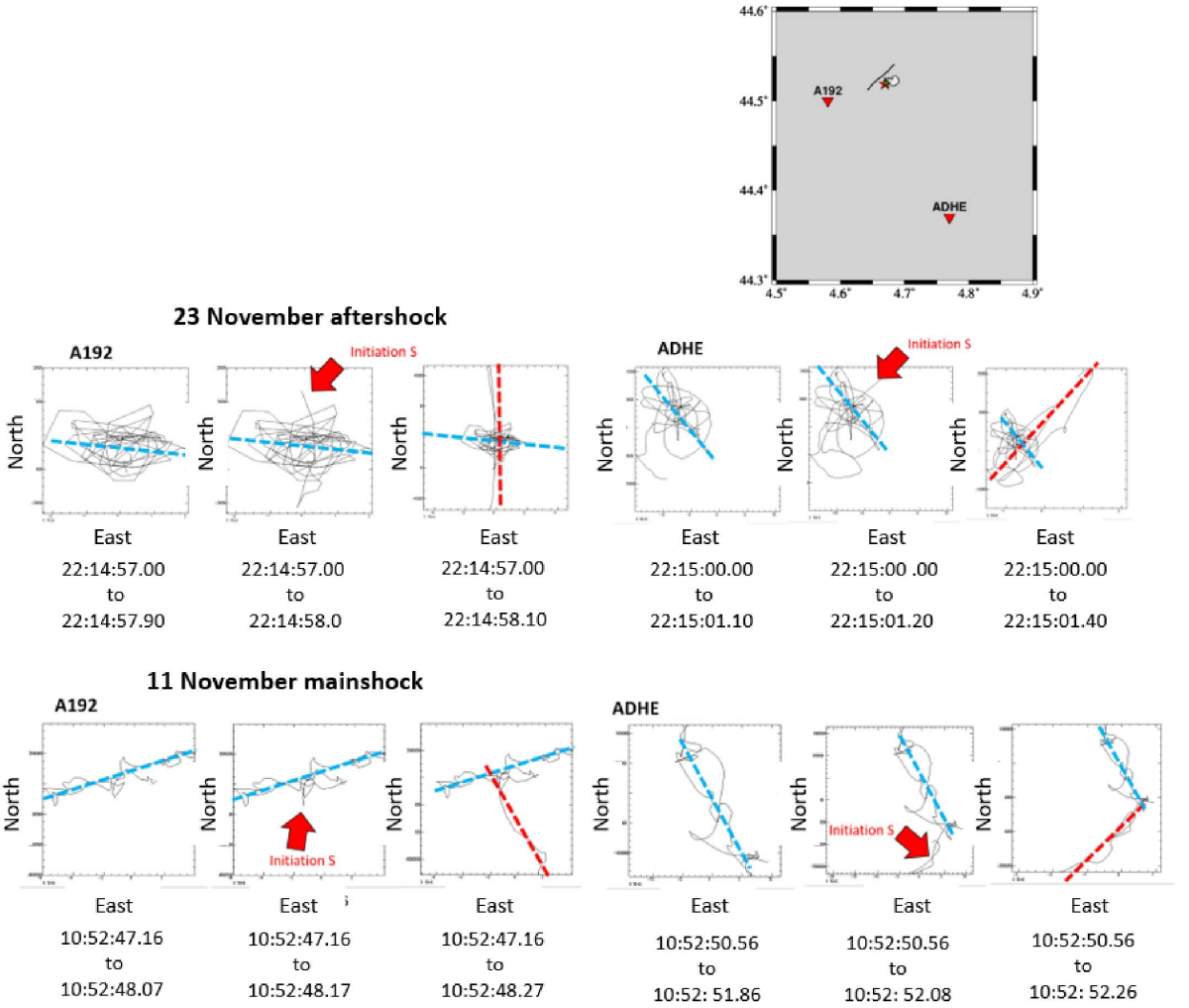

Supplementary Figure S1. Determination of the S-wave arrival time from the change of horizontal polarization (particle motion), example of stations A192 and ADHE. On top, map showing the position of the two stations (red triangles) with respect to the 11 November 2019 mainshock and 23 November 2019 aftershock epicenters (red and green stars, respectively). First row of graphs: mainshock. Second row of graphs: aftershock. Three graphs per station, with the time window indicated below (HH:MM:SS.SS). The blue dashed line shows the approximate dominant direction of particle motion in the coda of the P-wave just before the arrival of the S-wave. The big red arrow points to the initiation of a new direction of particle motion, interpreted as the initiation of the S-wave, i.e. corresponding approximately to the S-wave arrival time. The red dashed line shows the particle motion of the S-wave once it is well developed.

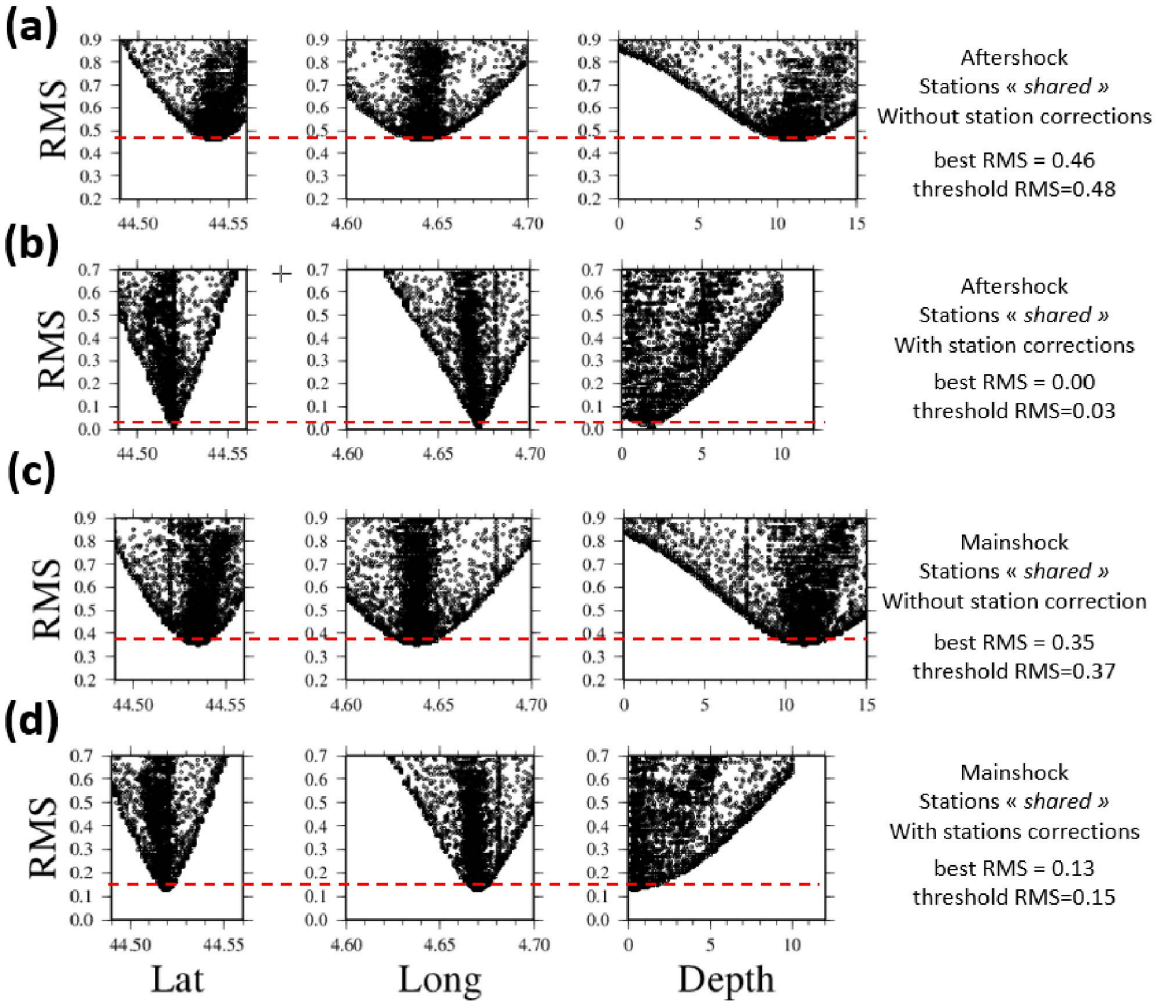

Supplementary Figure S2. Distribution of RMS misfit values as a function latitude, longitude and depth (km). These graphs are related to the strategy one "Master event" presented in Figure 2 of the paper. The red dashed line indicates the threshold in RMS used to display hypocentral solutions (those below the threshold).

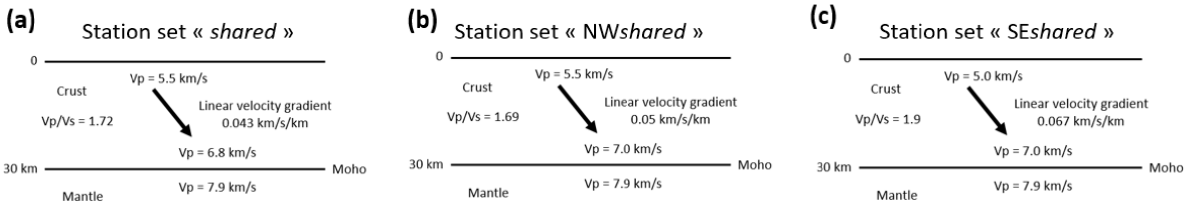

Supplementary Figure S3. Linear gradient velocity models found in strategy 2 "Dual velocity model" presented in Figure 5 of the paper.

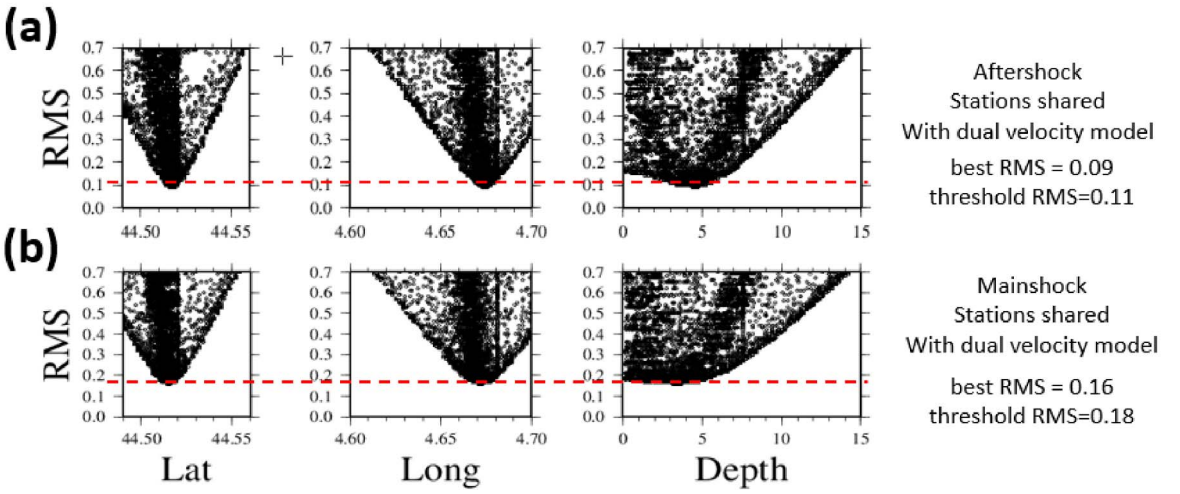

Supplementary Figure S4. Distribution of RMS misfit values as a function latitude, longitude and depth (km). These graphs are related to the strategy one "Dual velocity model" presented in Figure 5 of the paper. The red dashed line indicates the threshold in RMS used to display hypocentral solutions (those below the threshold).

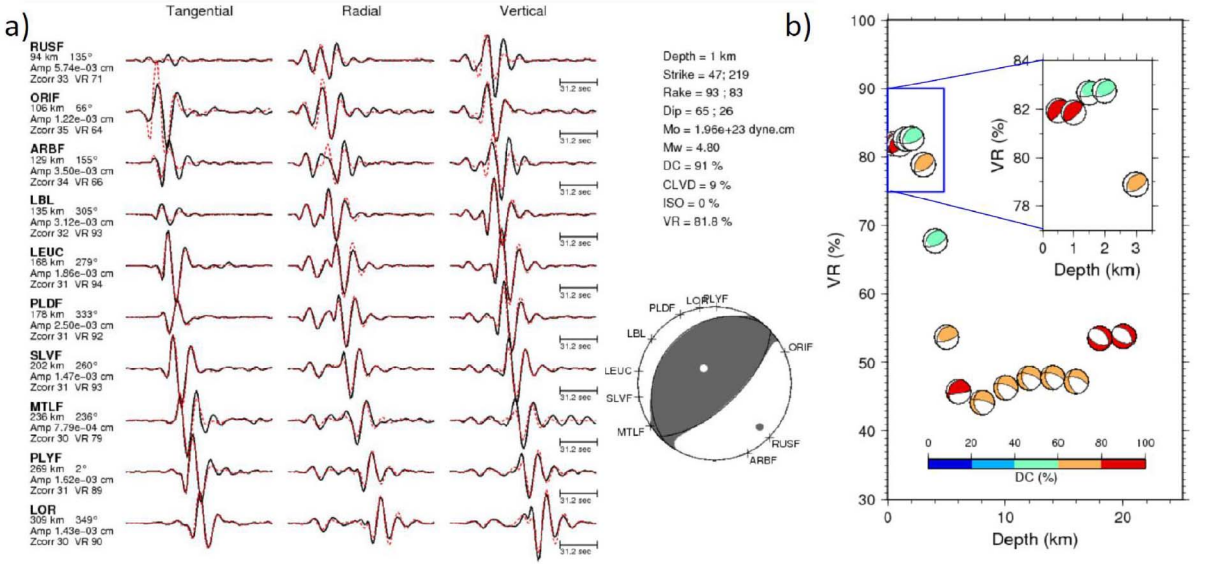

Supplementary Figure S5. Result of the TDMT waveform inversion. (a) Waveform modeling and source parameters. (b) Plot of focal mechanism solutions in a variance reduction (VR) versus depth graph. Color scale function of the % of double couple component (DC). Inset frame: zoom on the shallowest depth interval where the best solutions are found. Best solutions, with VR values between 82 and 83%, are found for depth smaller or equal to 2 km. The highest % of DC component is found at 1 km, which is considered as the preferred depth given that at 1.5 and 2 km the DC decreases below 60%. Modified from Vallage et al., in press.

Supplementary Table S1. Residuals at stations "shared" associated with the reference hypocenter of the 23 November aftershock obtained with the optimum local velocity model. These residuals constitute the station corrections used in the master event approach. STA: station name; DIST: epicentral distance in km; AZM: azimuth; AN: incidence with respect to the vertical; P/S: wave type; SEC: observed arrival time; TOBS: arrival time – origin time; TCAL: travel time in the model; RES: residual

STA NET COM L CR	DIST	AZM	AN	P/S	SEC	(TOBS	−TCAL	−DLY	=RES)
A192	8.0	255	98	P	56.27	1.65	1.78	0.00	−0.13
				S	57.94	3.32	3.22	0.00	0.10
CRU1	14.6	28	90	P	57.64	3.02	3.23	0.00	−0.21
				S	60.51	5.89	5.85	0.00	0.04
ADHE	18.0	154	87	P	58.12	3.50	3.95	0.00	−0.45
				S	61.14	6.52	7.15	0.00	−0.63*
OGDF	31.8	82	80	P	60.73	6.11	6.97	0.00	−0.86*
				S	66.42	11.80	12.62	0.00	−0.82*
BANN	44.3	248	73	P	62.61	7.99	9.58	0.00	−1.59*
A184	44.9	338	73	P	62.49	7.87	9.66	0.00	−1.79*
				S	68.12	13.50	17.48	0.00	−3.98*

Supplementary Table S2. Velocity models used in the FMNEAR waveform inversion of the Le Teil mainshock. H: layer thickness in km; V_p: P wave velocity in km/s; V_s: S wave velocity in km/s; ρ: density in g/cm^3; Q_p and Q_s: quality factor for the P and S waves respectively

Standard FMNEAR model (solution mentioned but not shown in the paper)					
H	V_p	V_s	ρ	Q_p	Q_s
0.60	3.30	1.90	2.00	200	100
1.40	4.50	2.60	2.30	350	175
3.00	5.50	3.18	2.50	500	250
25.00	6.50	3.75	2.90	600	300
Mantle	8.10	4.68	3.30	1000	500
Dual velocity model (used for the preferred solution shown in Figure 10)					
NW velocity model ($V_p/V_s = 1.69$ in the crust)					
H	V_p	V_s	ρ	Q_p	Q_s
7.50	5.50	3.25	2.40	450	225
7.50	6.00	3.55	2.55	500	250
7.50	6.50	3.85	2.75	600	300
7.50	7.00	4.14	2.90	700	350
Mantle	7.90	4.57	3.20	1000	500
SE velocity model ($V_p/V_s = 1.9$ in the crust)					
H	V_p	V_s	ρ	Q_p	Q_s
7.50	5.00	2.63	2.40	400	200
7.50	5.60	2.95	2.50	500	250
7.50	6.30	3.32	2.70	600	300
7.50	7.00	3.68	2.90	700	350
Mantle	7.90	4.57	3.20	1000	500

Supplementary Table S3. Filtering used in the FMNEAR inversion. STAT: station name; inst: instrument (vel: broadband velocimeter; acc: strong motion accelerometer); $f_{\min}$: lowcut frequency; $f_{\max}$: highcut frequency

STAT	inst	$f_{\min}$	$f_{\max}$
A183	vel	0.0500 Hz	0.1500 Hz
A184	vel	0.0500 Hz	0.1500 Hz
BALS	vel	0.0500 Hz	0.1500 Hz
BANN	vel	0.0800 Hz	0.1800 Hz
CRU1	acc	0.1500 Hz	0.3000 Hz
LAJA	vel	0.0500 Hz	0.1500 Hz
OGCC	vel	0.0700 Hz	0.1200 Hz
OGCN	vel	0.0500 Hz	0.0800 Hz
OGDF	vel	0.0700 Hz	0.1700 Hz
ORIF	vel	0.0500 Hz	0.0800 Hz
RUSF	vel	0.0400 Hz	0.0900 Hz
SAUF	vel	0.0400 Hz	0.0900 Hz
SSB	vel	0.0500 Hz	0.1500 Hz

Supplementary Table S4. Velocity models used in the TDMT waveform inversion of the Le Teil mainshock (Figure S5). H: layer thickness in km; V_p: P wave velocity in km/s; V_s: S wave velocity in km/s; ρ: density in g/cm^3; Q_p and Q_s: quality factor for the P and S waves respectively. From Duverger et al. [2021]

CEA/LDG Model					
H	V_p	V_s	ρ	Q_p	Q_s
0.9	3.00	1.73	2.7	200	61
25	6.03	3.56	2.7	300	128
Mantle	8.16	4.65	3.3	1000	500[2]

Supplementary Material on Section 5. Relative location of the mainshock with respect to a quarry blast

The arrival time of a signal at the ith station, T_i, is:

$$T_i = T_0 + TT_i$$

where T_0 is the origin time and TT_i is the P-wave travel time. Writing the above equation for the two events and then taking the difference, the difference between the arrival times of the two events is:

$$\Delta T_i = \Delta T_0 + \Delta TT_i$$

We take all the differences as mainshock minus blast. Assuming that the source separation is much shorter than the source-to-station ray paths, the travel time difference, ΔTT_i, is related to the spatial difference, $\Delta\vec{x}$, between the blast and mainshock hypocenters by the following linearized equation:

$$\Delta TT_i = \frac{1}{V_p}\overrightarrow{TOV}_i \cdot \Delta\vec{x}$$

where V_p denotes the P-wave velocity at a reference hypocenter location and, $\overrightarrow{TOV}_i$, the take-off vector on the P-wave ray leaving the reference hypocenter for the ith station. We assumed a depth of 1.3 km for the reference hypocenter and the same epicenter as the blast location. Our additional analyses using different depth values suggest a minor impact of this assumption on the results. For the calculation of the take-off angles, we used the refined local velocity profile found in Section 3 of the article, namely the optimum local velocity model (Figure 3d), and the DEPTABLE software (Lin and Shearer, 2006). Table S5 below summarizes the take-off angles and azimuth values for each station. The convention that we used for the computation of take-off vectors is clockwise from vertical down.

The linear relocation problem is then written in the usual form of a linear inverse problem: $Gm = d$, where G is a matrix of size $N \times 4$ (N is the number of stations) whose ith row contains $(1/V_p)\overrightarrow{TOV}_i$ in the first 3 columns and 1 in the last column, the model vector m is a 4-D vector composed of the unknowns $\Delta\vec{x}$ and ΔT_0, and the data vector d is the vector of N differential arrival times ΔT_i. We solved the problem multiple times (50,000 realizations), by weighted least-squares minimization, each time taking a new random sample of arrival times T_i from Gaussian distributions representing the central value and width of the P-wave pick range at each station. This random sampling results in a set of mainshock hypocenter locations, out of which we opt for those consistent with our priors on the fault trace location and dip angle.

Supplementary Table S5. Distance to blasting zone, azimuth, and take-off angle for each station

Station name	Distance to blasting zone (km)	Azimuth (degree)	Take-off angle (degree)
A192B	8.5	252.90	85.09
ADHE	18.0	155.87	93.84
OGDF	31.0	82.90	109.27
A184A	45.0	336.67	117.46
11	25.0	169.65	105.38
19	25.0	173.44	105.38
26	18.0	155.87	93.84

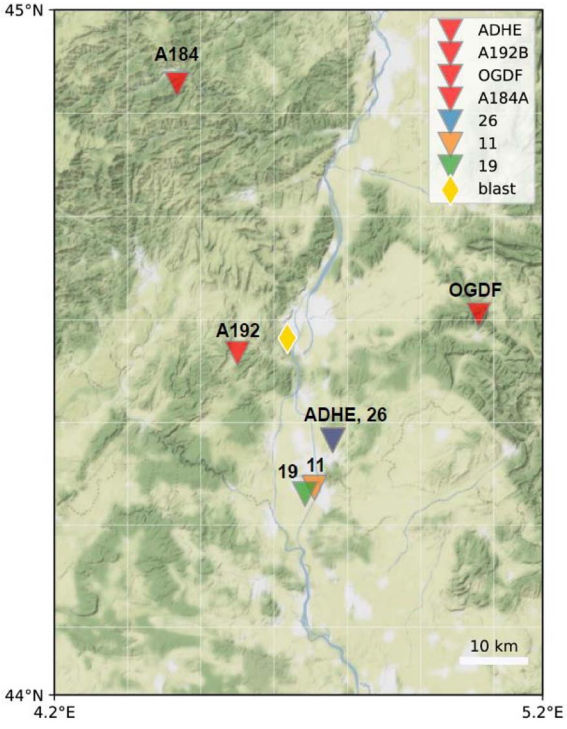

Supplementary Figure S6. Map of stations used for the relative location of the mainshock with respect to a quarry blast. Nearby stations ADHE and 26 are superimposed on the map. Golden diamond denotes the blasting location.

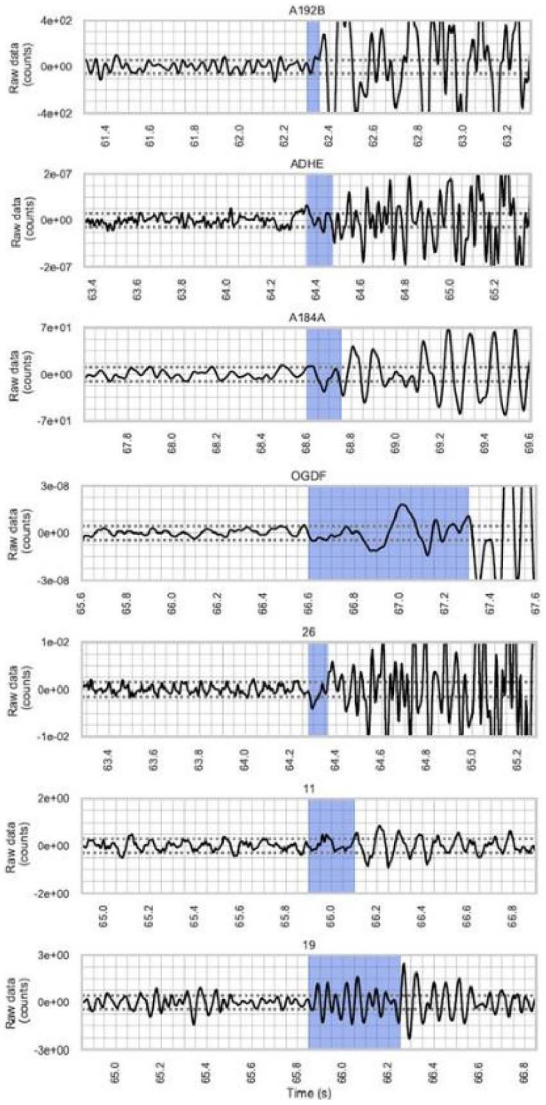

Supplementary Figure S7. Time picks for blast signals at each station. Station names are given in subplot titles. Shadowed areas correspond to the range of time picks of our analysis. Start time is a minute prior to the catalogued event time: 2019-11-08T10:05:27.

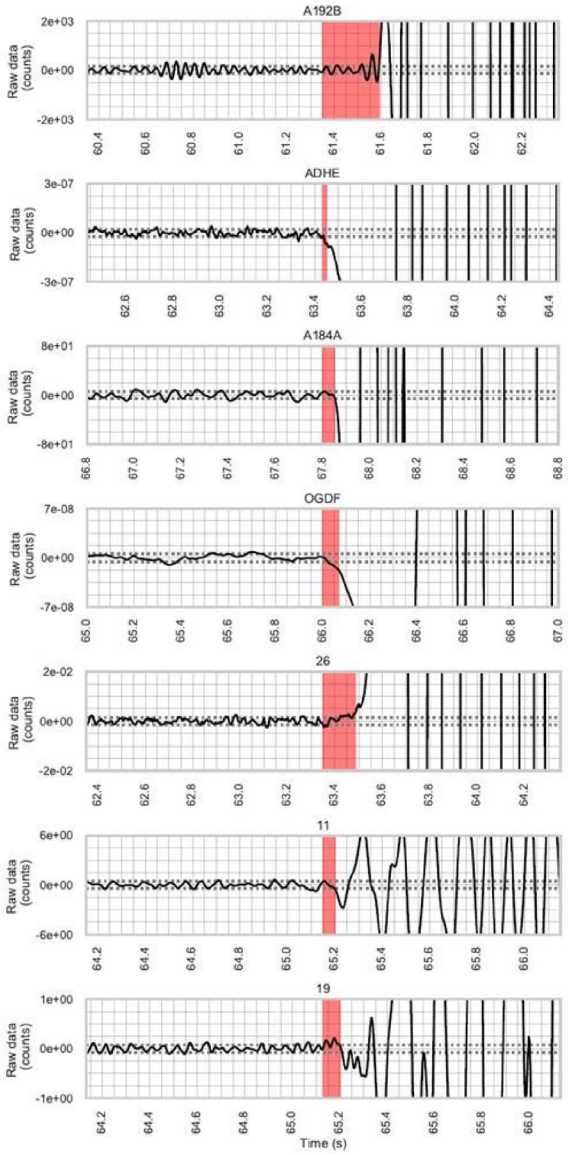

Supplementary Figure S8. Time picks for mainshock signals at each station. Station names are given in subplot titles. Shadowed areas correspond to the range of time picks of our analysis. Start time is a minute prior to the catalogued event time: 2019-11-11T10:51:45.

Supplementary Table S6. Polarity data used for the focal mechanisms of the mainshock. STA: station name; AZ: azimuth; INC: incidence; POL: polarity, 1 = compression, −1 – dilatation; NET: Network. If the seismic ray initially points upward, it has been transformed into a downward plunging ray for the stereographic representation. Station names may be truncated if they contain more than four letters. Networks explanation: FR: RESIF and other broad-band and accelerometric permanent networks in metropolitan France; RA: Réseau Accélérométrique Permanent (French Accelerometrique Network); AlpArray: AlpArray, Hetényi et al., 2018; IRSN: Institut de Radioprotection et de Sûreté Nucléaire; 3C: M5 Le Teil 20191111 PostSeismic stations from various organisms available through RESIF portal; G: GEOSCOPE; MT: French Landslide Observatory/OMIV: Permanent seismological records on unstable slopes; MN: Mediterranean Very Broadband Seismographic Network; GU: Regional Seismic Network of North Western Italy; IV: Italian National Seismic Network; RD: CEA/DASE Seismic Network; CH: Switzerland Seismological Network; LC: LSC (Laboratorio Subterraneo Canfranc); II: Global Seismograph Network – IRIS/IDA; SI: Province Südtirol; OE: Austrian Seismic Network

STA	AZ	INC	POL	NET
CRU1	28.0	88.0	1.	3C
NO30	186.0	87.0	-1.	IRSN
ADHE	153.0	86.0	-1.	3C
PAUL	164.0	85.0	-1.	3C
NO25	173.0	84.0	-1.	IRSN
NO27	183.0	84.0	-1.	IRSN
OGLP	176.0	83.0	-1.	RA
NO28	182.0	82.0	-1.	IRSN
BOLL	170.0	82.0	-1.	3C
NO22	162.0	82.0	-1.	IRSN
NO21	165.0	81.0	-1.	IRSN
NO20	169.0	81.0	-1.	IRSN
OGDF	82.0	79.0	-1.	FR
BANN	249.0	73.0	1.	FR
A184	338.0	73.0	-1.	AlpArray
OGCB	42.0	71.0	1.	FR
OGCC	97.0	63.0	-1.	FR
SAUF	151.0	61.0	-1.	FR
OGCN	24.0	60.0	1.	FR
SSB	354.0	57.0	1.	G
RUSF	134.0	56.0	-1.	FR
AVR	57.0	55.0	1.	MT
AVP	59.0	55.0	1.	MT
AVM	59.0	55.0	1.	MT
CLAU	164.0	40.0	1.	Private
A191	257.0	55.0	1.	AlpArray
A183	305.0	54.0	1.	AlpArray
BALS	271.0	54.0	1.	FR
A180	331.0	35.0	-1.	AlpArray

(continued on next page)

Supplementary Table S6. (continued)

STA	AZ	INC	POL	NET
MLYF	123.0	35.0	-1.	FR
ORIF	64.0	35.0	1.	FR
OGS2	55.0	35.0	1.	FR
A187	284.0	35.0	1.	AlpArray
A215	23.0	35.0	1.	AlpArray
BSTF	135.0	35.0	-1.	FR
OGLC	97.0	35.0	-1.	FR
GRN	46.0	35.0	1.	FR
A177	358.0	35.0	1.	AlpArray
BLAF	119.0	35.0	-1.	FR
LAJA	243.0	35.0	1.	FR
OGDI	109.0	35.0	1.	FR
COLF	326.0	35.0	1.	FR
OCSF	296.0	35.0	1.	RA
ARTF	138.0	35.0	-1.	FR
A176	341.0	35.0	1.	AlpArray
OGSM	33.0	35.0	1.	FR
OGAG	77.0	35.0	1.	FR
OCOL	329.0	35.0	1.	RA
OGCH	39.0	35.0	1.	RA
A182	290.0	35.0	1.	AlpArray
A181	52.0	35.0	1.	AlpArray
A175	11.0	35.0	1.	AlpArray
TRIG	121.0	35.0	-1.	FR
A174	355.0	35.0	1.	AlpArray
A195	250.0	35.0	1.	AlpArray
BNI	68.0	35.0	1.	MN
LEUC	280.0	35.0	1.	FR
SURF	90.0	35.0	1.	FR
A179	309.0	35.0	1.	AlpArray
RRL	74.0	35.0	1.	GU
ENAU	104.0	35.0	1.	FR
OGMO	63.0	35.0	1.	FR
OGMY	31.0	35.0	1.	FR
PLDF	334.0	35.0	1.	FR
A198	237.0	35.0	1.	AlpArray
A178	44.0	35.0	1.	AlpArray
OG35	22.0	35.0	1.	FR
CFF	320.0	35.0	1.	FR

(continued on next page)

Supplementary Table S6. (continued)

STA	AZ	INC	POL	NET
OGAN	36.0	35.0	1.	RA
A171	348.0	35.0	1.	AlpArray
FRNF	301.0	35.0	1.	FR
ISO	100.0	35.0	1.	FR
PZZ	89.0	35.0	1.	GU
RSL	49.0	35.0	1.	FR
OGRV	1.0	35.0	1.	FR
AGO	326.0	35.0	1.	FR
MVIF	108.0	35.0	-1.	FR
SPIF	103.0	35.0	-1.	FR
A172	12.0	35.0	1.	AlpArray
OG02	33.0	35.0	1.	FR
A170	336.0	35.0	1.	AlpArray
A169	359.0	35.0	1.	AlpArray
MRGE	52.0	35.0	1.	IV
MTLF	238.0	35.0	1.	RD
PIAF	99.0	35.0	1.	FR
REMY	52.0	35.0	1.	GU
A167	11.0	35.0	1.	AlpArray
A173	37.0	35.0	1.	AlpArray
CIRO	61.0	35.0	1.	GU
A166	352.0	35.0	1.	AlpArray
MONQ	268.0	35.0	1.	FR
SENI	44.0	35.0	1.	CH
BRAN	26.0	35.0	1.	CH
CHMF	26.0	35.0	1.	FR
FIES	50.0	35.0	1.	CH
A160	4.0	35.0	1.	AlpArray
MUGI	64.0	35.0	1.	CH
RONF	22.0	35.0	1.	FR
A158	17.0	35.0	1.	AlpArray
CHIF	297.0	35.0	1.	FR
ECH	24.0	35.0	1.	FR
CANF	247.0	35.0	1.	LC
SLE	37.0	35.0	1.	CH
FUOR	59.0	35.0	1.	CH
BRMO	61.0	35.0	1.	IV
BFO	32.0	35.0	1.	II
LUSI	69.0	35.0	1.	SI

(continued on next page)

Supplementary Table S6. (continued)

STA	AZ	INC	POL	NET
CIEL	22.0	35.0	1.	FR
FETA	57.0	35.0	1.	OE
LEMB	24.0	35.0	1.	FR
MOTA	55.0	35.0	1.	OE
SQTA	57.0	35.0	1.	OE
WTTA	58.0	35.0	1.	OE
BEGF	306.0	35.0	1.	FR

Supplementary Table S7. Polarity data used for the focal mechanisms of the aftershock. STA: station name; AZ: azimuth; INC: incidence; POL: polarity, 1 = compression, −1 – dilatation; NET: Network. If the seismic ray initially points upward, it has been transformed into a downward plunging ray for the stereographic representation. Station names may be truncated if they contain more than four letters. See Table S6 for networks explanation

STA	AZ	INC	POL	NET
N10	50.0	25.0	1.	3C
LAFA	43.0	26.0	1.	3C
N07	152.0	31.0	-1.	3C
N04	101.0	35.0	-1.	3C
N08	308.0	38.0	1.	3C
N25	308.0	38.0	1.	3C
N27	309.0	38.0	1.	3C
N09	63.0	40.0	-1.	3C
N03	88.0	45.0	-1.	3C
XX03	194.0	49.0	-1.	3C
N26	73.0	50.0	-1.	3C
N05	152.0	57.0	-1.	3C
N01	31.0	58.0	1.	3C
N12	74.0	57.0	-1.	3C
N14	73.0	58.0	-1.	3C
N15	74.0	58.0	-1.	3C
N13	74.0	58.0	-1.	3C
N11	73.0	58.0	-1.	3C
XX02	353.0	63.0	-1.	3C
TEIL	196.0	64.0	-1.	3C
ILES	260.0	66.0	-1.	3C
N02	95.0	67.0	-1.	3C
STIL	95.0	67.0	-1.	3C
CROT	63.0	67.0	-1.	3C

(continued on next page)

Supplementary Table S7. (continued)

STA	AZ	INC	POL	NET
THOM	59.0	67.0	-1.	3C
N21	136.0	68.0	-1.	3C
N20	340.0	70.0	-1.	3C
N17	340.0	70.0	-1.	3C
N19	340.0	70.0	-1.	3C
N28	340.0	70.0	-1.	3C
N22	134.0	69.0	-1.	3C
N06	137.0	69.0	-1.	3C
N24	137.0	69.0	-1.	3C
N23	139.0	69.0	-1.	3C
VIVI	340.0	70.0	-1.	3C
N16	50.0	74.0	-1.	3C
N18	135.0	74.0	-1.	3C
ALBA	126.0	77.0	-1.	3C
AUBI	149.0	78.0	-1.	3C
A192	75.0	81.0	-1.	AlpArray
MONN	221.0	83.0	1.	3C
LARN	38.0	83.0	1.	3C
ADHE	154.0	88.0	-1.	3C
BANN	248.0	74.0	1.	FR
A184	338.0	73.0	1.	AlpArray
OGCB	42.0	71.0	1.	FR
SSB	354.0	58.0	1.	G
A180	331.0	35.0	1.	AlpArray